Supplement of Hydrol. Earth Syst. Sci., 30, 2913–2930, 2026
https://doi.org/10.5194/hess-30-2913-2026-supplement
© Author(s) 2026. CC BY 4.0 License.

Hydrology and Earth System Sciences
Open Access
EGU

Supplement of

Increasing daily precipitation extremes despite declining annual totals in southern Europe: a modeling study on the effects of Mediterranean Sea warming

Alfonso Senatore et al.

Correspondence to: Alfonso Senatore (alfonso.senatore@unical.it)

The copyright of individual parts of the supplement might differ from the article licence.

Figure S1 shows the results of a trend analysis applied to 134 historical gauges of the regional monitoring network stations (Fig. 1a in the main text) using the non-parametric trend tests of Mann-Kendall (identifying significance at a 5% level) and Sen's slope estimator (determining the trend slope per year), employed to analyze long-time (from 1955 to 2023) hydro-climatic series of annual precipitation (PRCPTOT) and maximum one-day precipitation (RX1day) in the wet season. To estimate missing daily values or reconstruct detected outliers, a linear correlation process was applied as follows: (i) daily rainfall data were collected for each station from 1955 to 2023. If fewer than 15 days were missing in a given year (approximately 4%, as suggested in several studies, e.g., Aguilar et al. 2005; Donat et al. 2013; Stephenson et al. 2014), the dataset for that year was considered complete. (ii) If more than 15 days were missing for a station in a given year, we performed a linear regression between that station's available data and the data from a nearby station with a strong correlation (always above 0.8, often much higher). The regression equation was then used to fill the gaps. While this approach could influence extreme-event values, we applied it cautiously, taking into account the characteristics of the data.

Overall, for PRCPTOT the decreasing trend is quite clear (105 stations with negative trends, 29 of which are significant), while for RX1day the positive trend is less pronounced (78 stations with positive trends, only 7 of which are significant, against only 4 significant negative trends). Nevertheless, it clearly indicates that trends in extreme precipitation differ from those in total precipitation, especially in some zones of the region (e.g., the south and east), which are more exposed to events from the Ionian Sea.

Table S1 lists the datasets used for the SST analysis described in the main text, while Table S2 outlines the physical parameterization scheme adopted for the WRF dynamical downscaling. Fig. S2 shows the accumulated precipitation associated with event no. 12, obtained by applying spectral nudging on the external domain D01 and considering both the reference (SST0) and perturbed (SST+3) sea surface temperature scenarios. Figures S3–S22 provide cumulative precipitation maps (mm) for each of the 20 events observed in the Calabria region, simulated under the SST0 configuration.

Table S3 provides a detailed analysis of the 20 precipitation events identified in the September-December 2019 period. It quantifies average precipitation (mm) across the entire internal domain of the WRF simulation, overland-only precipitation, and precipitation above the 95^{th} percentile, simulated by SST0, SST-1, and SST+3 scenarios, respectively.

Figure S23 reports the simulated center of mass for the 20 events across the three SST scenarios calculated over the domain D01. Figure S24 shows the cumulative precipitation for event no. 12 achieved by adopting a different PBL scheme (YSU, instead of MYJ) in the SST0 and SST+3 scenarios, respectively. Figure S25 depicts the column precipitable water and the sea level pressure over the D01 domain for a specific time related to events no. 6 and no. 15, by considering the three SST scenarios. Finally, Figures S26 and S27 show the average Convective Available Potential Energy (CAPE), horizontal wind, as well as vertical profiles of omega, wind, and water vapor mixing ratio for events no. 6 and no. 15, respectively, considering the three SST configurations. All simulations employed the WRF model, forced with ERA5 boundary conditions, utilizing two

one-way nested domains with a 2-km horizontal resolution of the innermost domain (the reader is referred to the main text for further details).

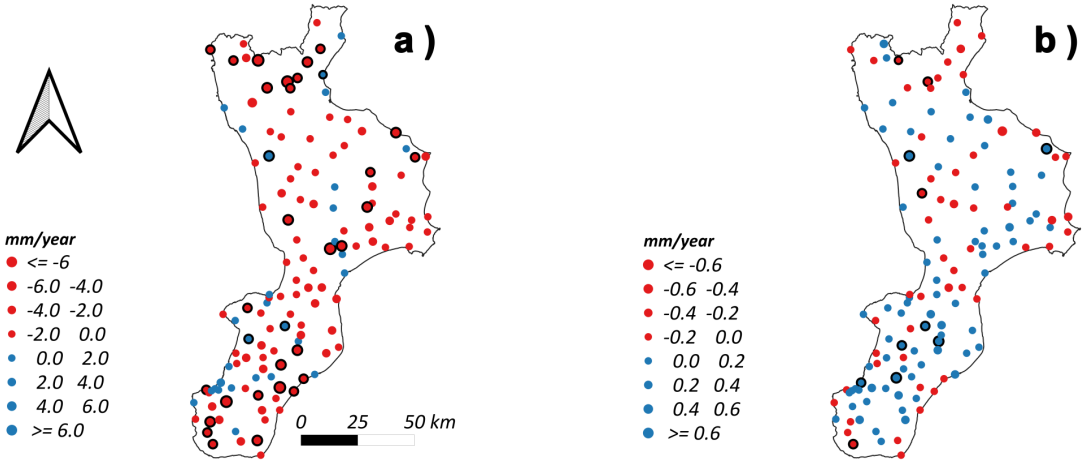

Figure S1. Mann-Kendall and Sen's slope tests for observations of a) PRCPTOT at annual scale, b) RX1day at wet season scale from September to February over Calabria from 1955 to 2023. Black-contoured dots indicate stations with statistically significant trends.

Table S1. List of datasets (IDs 0_1 and 0_2) and GCMs (IDs 1-22) considered for assessing observed/estimated historical and estimated future SST evolution in the Mediterranean Area. GCMs data have been provided by Instituto de Física de Cantabria (IFCA)

ID	Complete Name	Institution	Model	Variant	Reference
0_1	ERA5 Reanalysis	ECMWF	Reanalysis		Hersbach et al. (2020)
0_2	SST_GLO_SST_L4_REP_OBSERVATIONS_010_024	CMEMS	Observation		(CMEMS) (2023)
1	ACCESS-CM2_CSIRO-ARCCSS_r1i1p1f1	CSIRO-ARCCSS	ACCESS-CM2	r1i1p1f1	Dix et al. (2023)
2	ACCESS-ESM1-5_CSIRO_r1i1p1f1	CSIRO	ACCESS-ESM1-5	r1i1p1f1	Ziehn et al. (2023)
3	AWI-CM-1-1-MR_AWI_r1i1p1f1	AWI	AWI-CM-1-1-MR	r1i1p1f1	Semmler et al. (2023)
4	BCC-CSM2-MR_BCC_r1i1p1f1	BCC	BCC-CSM2-MR	r1i1p1f1	Xin et al. (2023)
5	CAMS-CSM1-0_CAMS_r2i1p1f1	CAMS	CAMS-CSM1-0	r2i1p1f1	Rong (2023)
6	CESM2-WACCM_NCAR_r1i1p1f1	NCAR	CESM2-WACCM	r1i1p1f1	Danabasoglu (2023)
7	CMCC-CM2-SR5_CMCC_r1i1p1f1	CMCC	CMCC-CM2-SR5	r1i1p1f1	Lovato and Peano (2023)
8	CNRM-CM6-1-HR_CNRM-CERFACS_r1i1p1f2	CNRM-CERFACS	CNRM-CM6-1-HR	r1i1p1f2	Voldoire (2023a)
9	CNRM-CM6-1_CNRM-CERFACS_r1i1p1f2	CNRM-CERFACS	CNRM-CM6-1	r1i1p1f2	Voldoire (2023b)
10	CNRM-ESM2-1_CNRM-CERFACS_r1i1p1f2	CNRM-CERFACS	CNRM-ESM2-1	r1i1p1f2	Seferian (2023)
11	CanESM5_CCCma_r1i1p1f1	CCCma	CanESM5	r1i1p1f1	Swart et al. (2023)
12	EC-Earth3_EC-Earth-Consortium_r1i1p1f1	EC-Earth-Consortium	EC-Earth3	r1i1p1f1	(EC-Earth)
13	FGOALS-g3_CAS_r1i1p1f1	CAS	FGOALS-g3	r1i1p1f1	Li (2023)
14	GFDL-ESM4_NOAA-GFDL_r1i1p1f1	NOAA-GFDL	GFDL-ESM4	r1i1p1f1	Krasting et al. (2023)
15	IITM-ESM_CCCR-IITM_r1i1p1f1	CCCR-IITM	IITM-ESM	r1i1p1f1	Panickal et al. (2023)
16	INM-CM5-0_INM_r1i1p1f1	INM	INM-CM5-0	r1i1p1f1	Volodin et al. (2023)
17	IPSL-CM6A-LR_IPSL_r1i1p1f1	IPSL	IPSL-CM6A-LR	r1i1p1f1	Boucher et al. (2023)
18	MPI-ESM1-2-HR_MPI-M_r1i1p1f1	MPI-M	MPI-ESM1-2-HR	r1i1p1f1	Jungclaus et al. (2023)
19	MPI-ESM1-2-LR_MPI-M_r1i1p1f1	MPI-M	MPI-ESM1-2-LR	r1i1p1f1	Wieners et al. (2023)
20	NorESM2-LM_NCC_r1i1p1f1	NCC	NorESM2-LM	r1i1p1f1	Seland et al. (2023)
21	NorESM2-MM_NCC_r1i1p1f1	NCC	NorESM2-MM	r1i1p1f1	Bentsen et al. (2023)
22	UKESM1-0-LL_MOHC_r1i1p1f2	MOHC	UKESM1-0-LL	r1i1p1f2	Tang et al. (2023)

Table S2. WRF physical schemes adopted.

Component	Scheme	References
Microphysics	New Thompson	Thompson et al. (2008)
PBL	MYJ	Janjić (1994)
Longwave	RTTM	Mlawer et al. (1997)
Shortwave	Goddard	Matsui et al. (2020)
Land Surface Model	NOAH-MP	Niu et al. (2011)
Cumulus	Tiedke (only D01)	Tiedtke (1989)
SST	sst_skin	Zeng and Beljaars (2005)

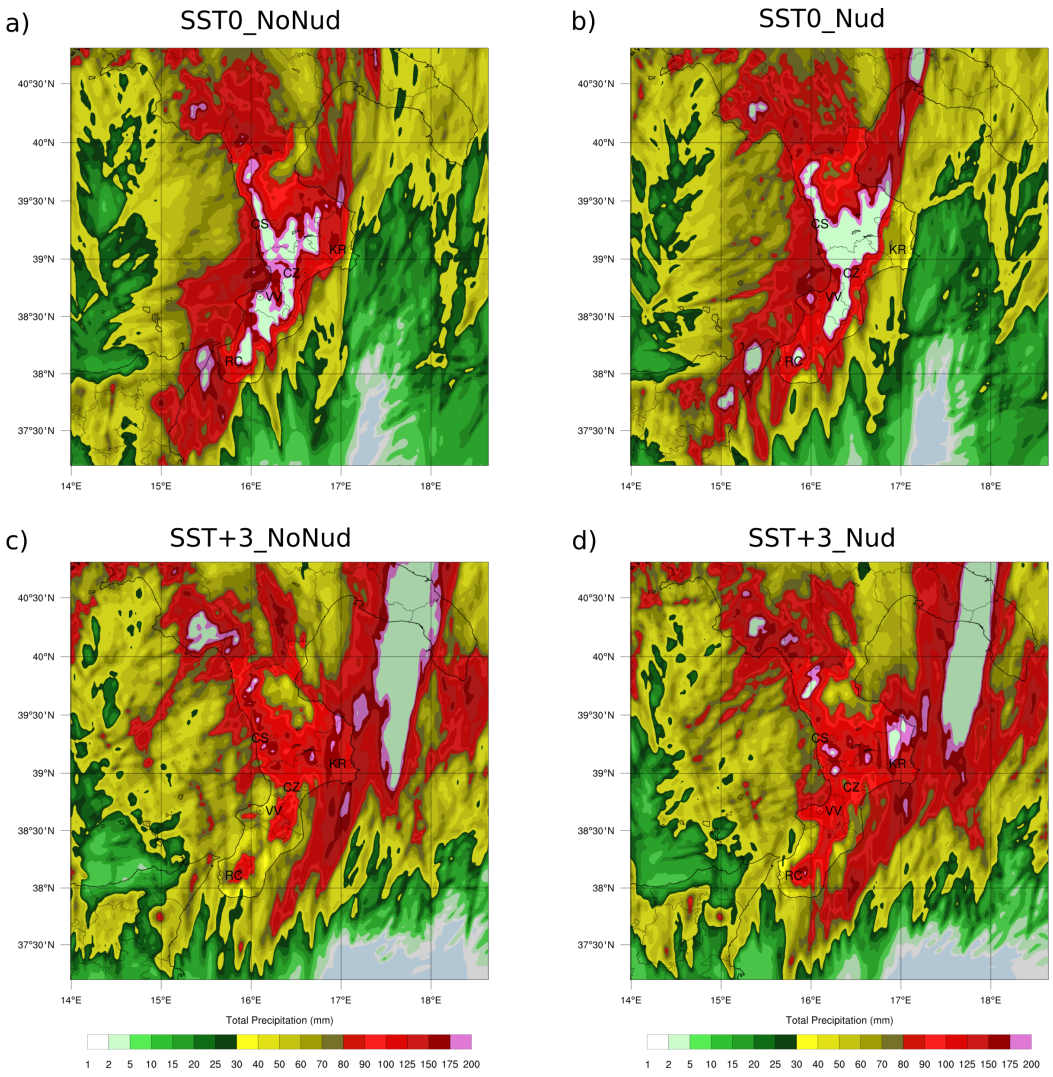

Figure S2. Cumulative precipitation for event no. 12 without (a, c) and with (b, d) nudging for the scenarios SST0 (a, b) and SST+3 (c, d).

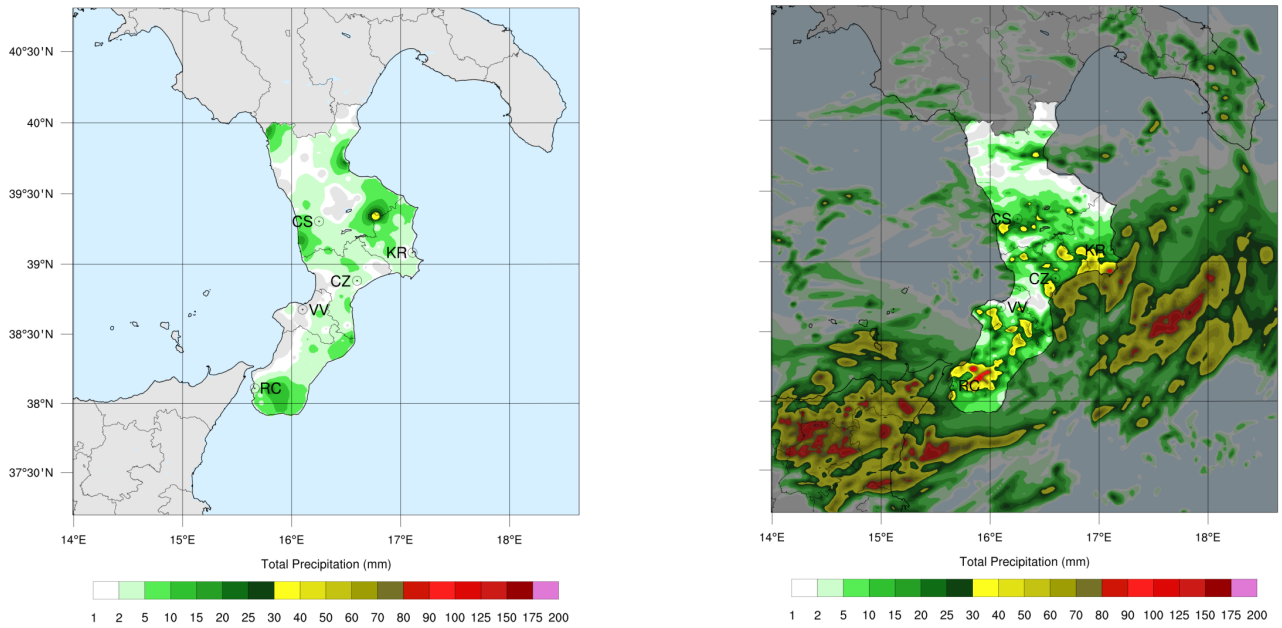

Figure S3. Cumulative precipitation for event 1: on the left, interpolated observation map; on the right, SST0 simulation.

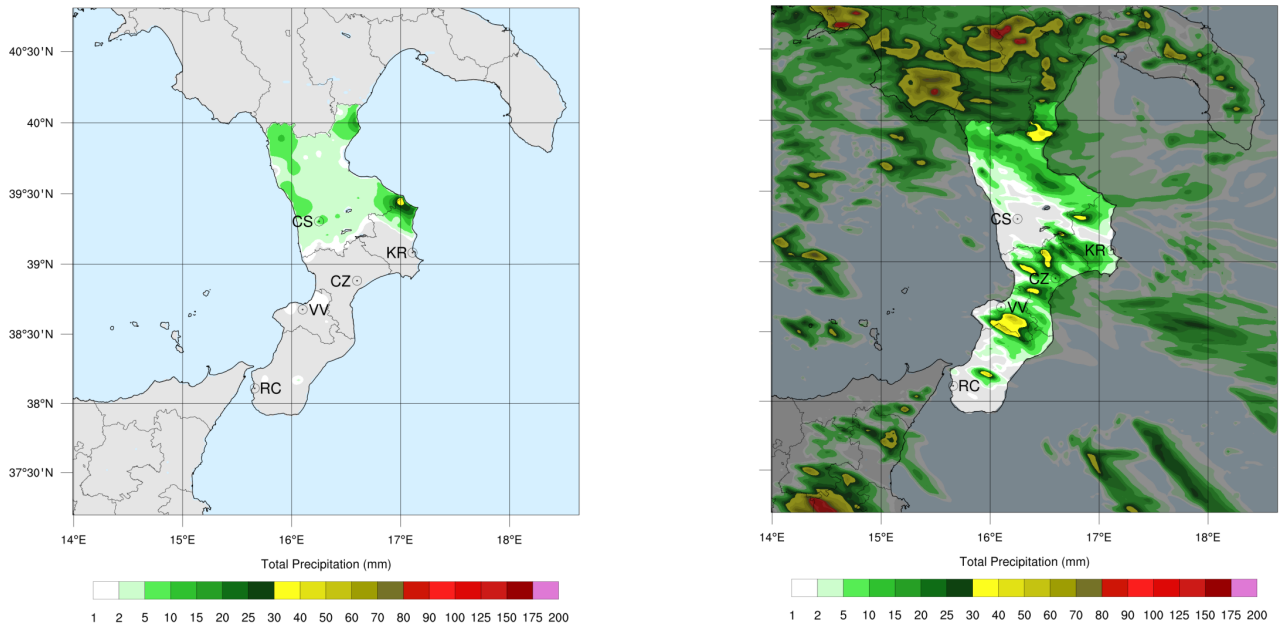

Figure S4. Cumulative precipitation for event 2: on the left, interpolated observation map; on the right, SST0 simulation.

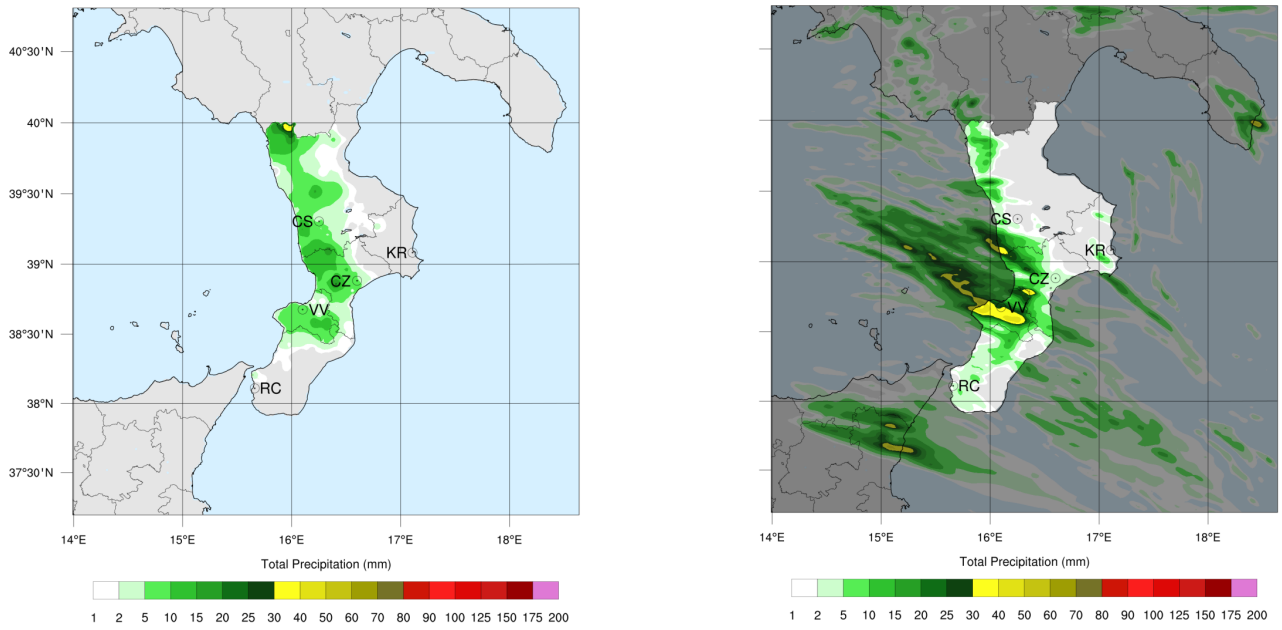

Figure S5. Cumulative precipitation for event 3: on the left, interpolated observation map; on the right, SST0 simulation.

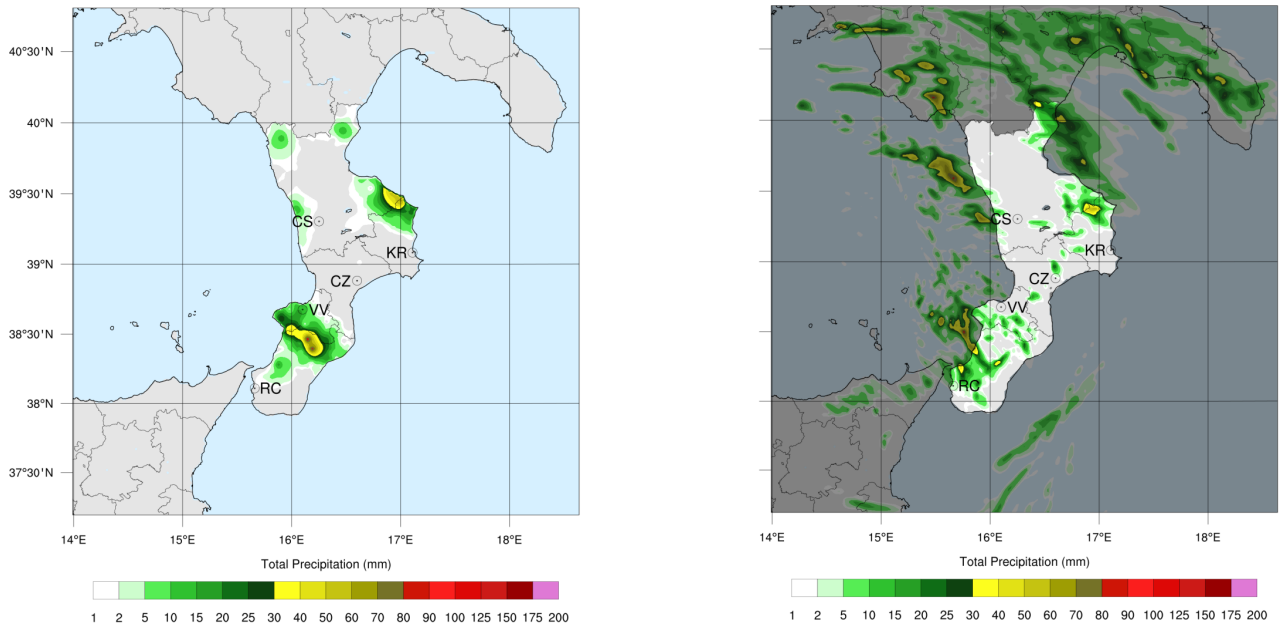

Figure S6. Cumulative precipitation for event 4: on the left, interpolated observation map; on the right, SST0 simulation.

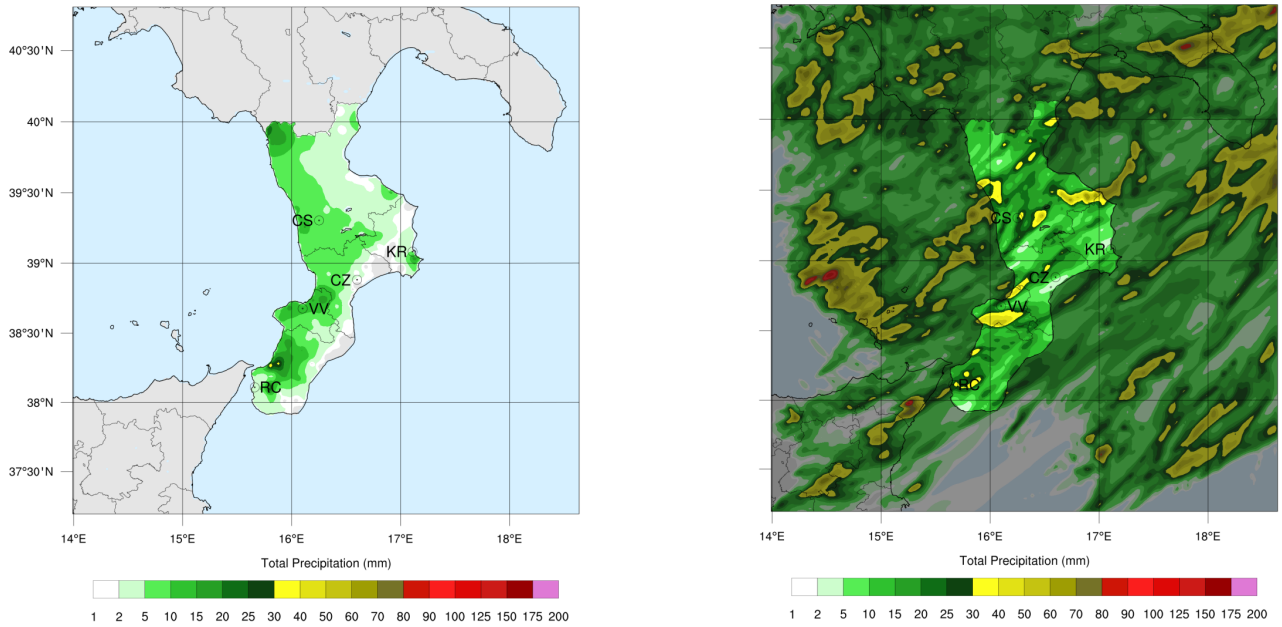

Figure S7. Cumulative precipitation for event 5: on the left, interpolated observation map; on the right, SST0 simulation.

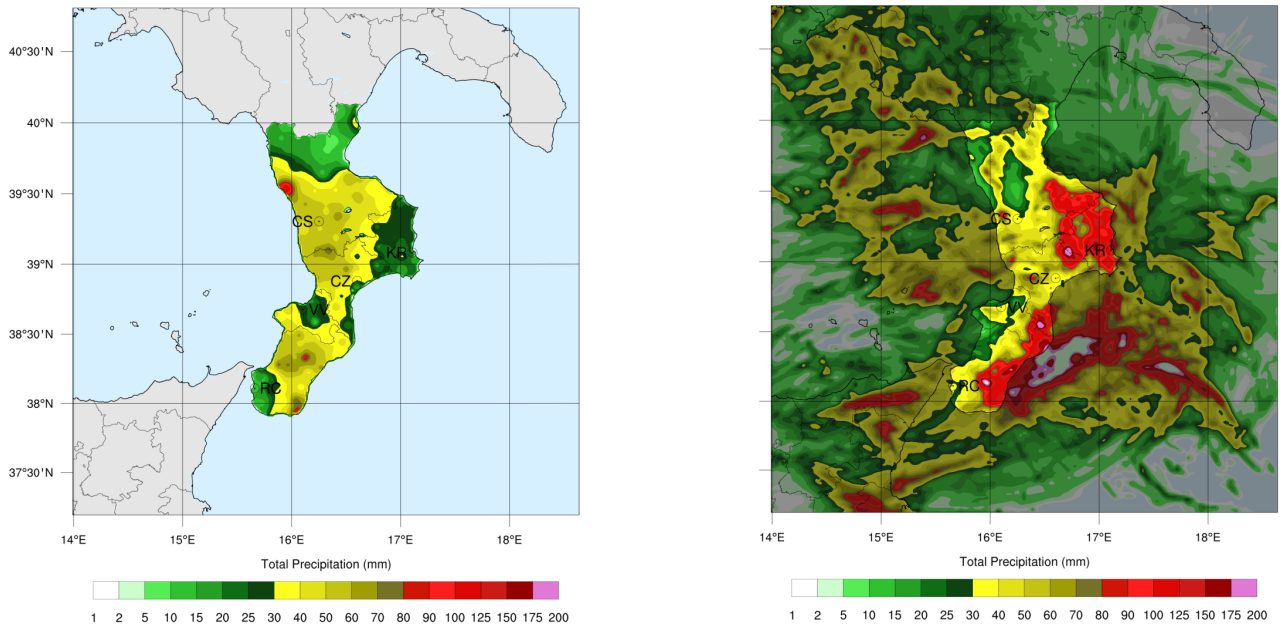

Figure S8. Cumulative precipitation for event 6: on the left, interpolated observation map; on the right, SST0 simulation.

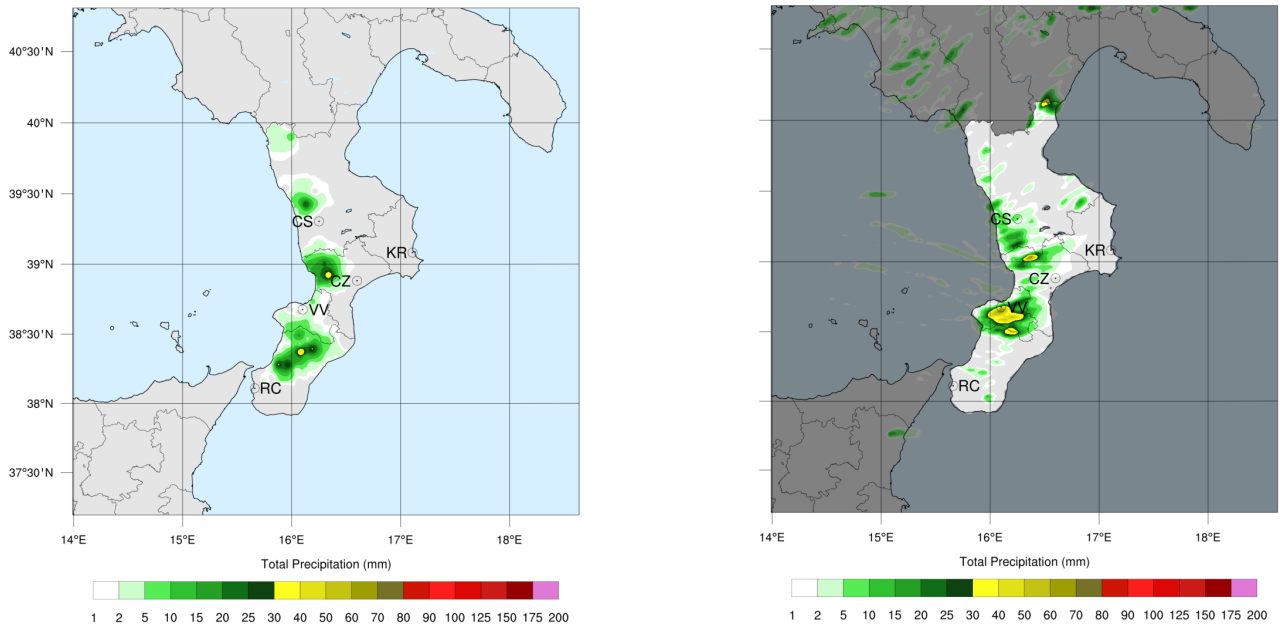

Figure S9. Cumulative precipitation for event 7: on the left, interpolated observation map; on the right, SST0 simulation.

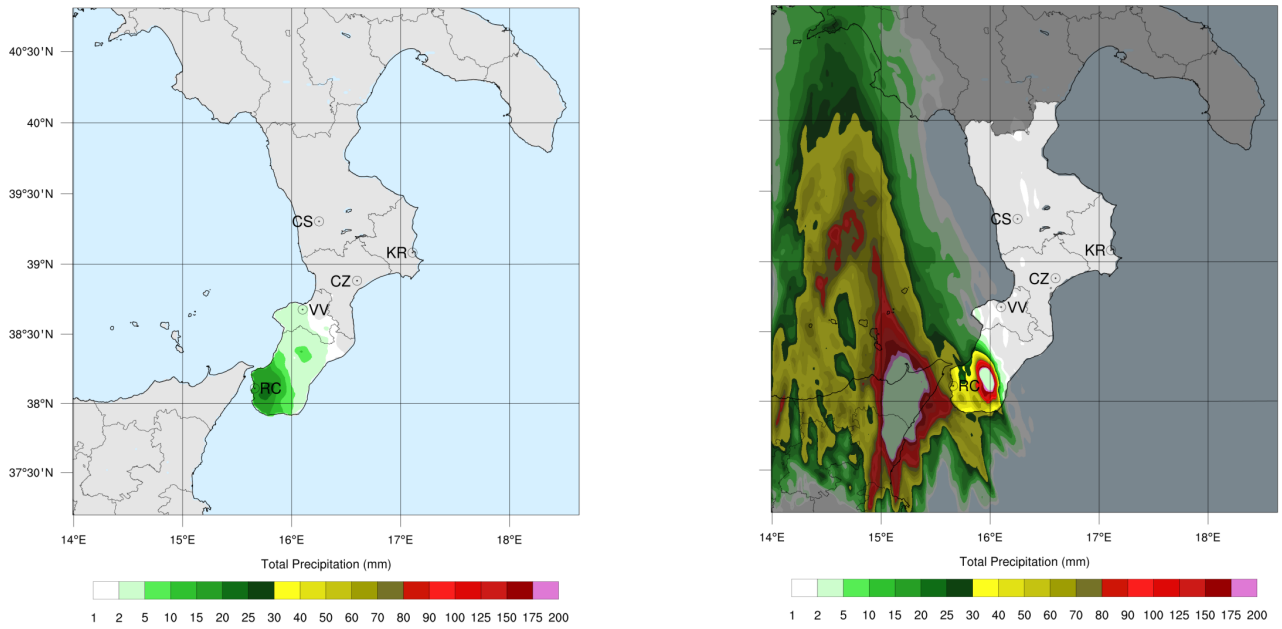

Figure S10. Cumulative precipitation for event 8: on the left, interpolated observation map; on the right, SST0 simulation.

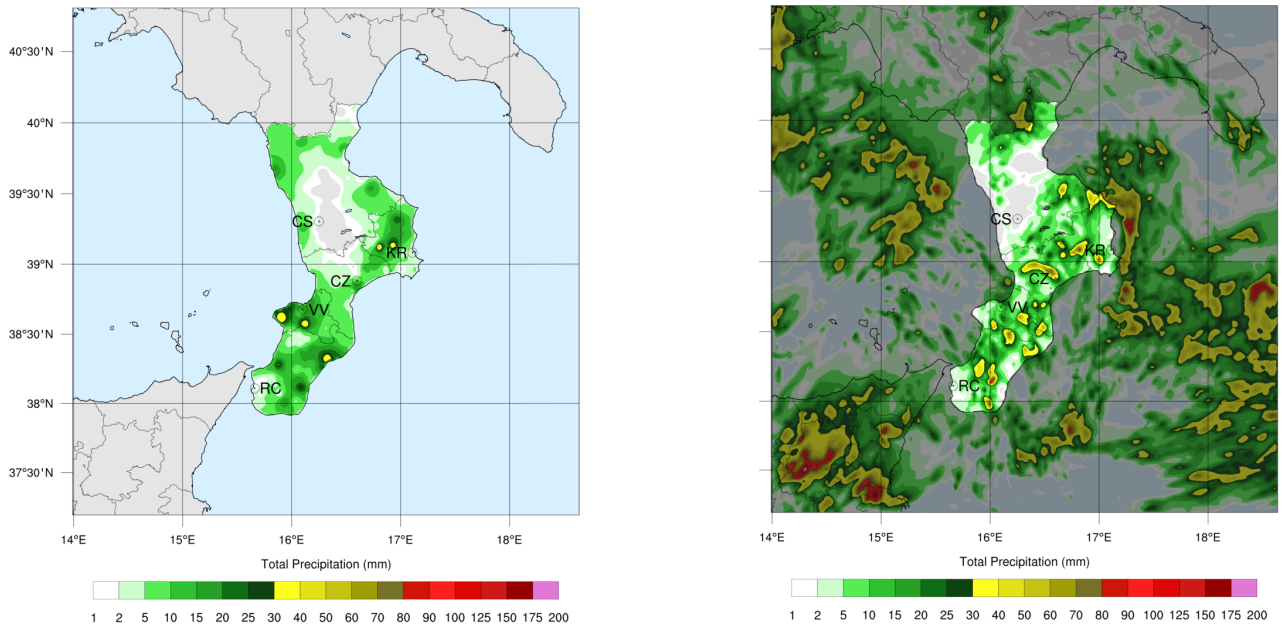

Figure S11. Cumulative precipitation for event 9: on the left, interpolated observation map; on the right, SST0 simulation.

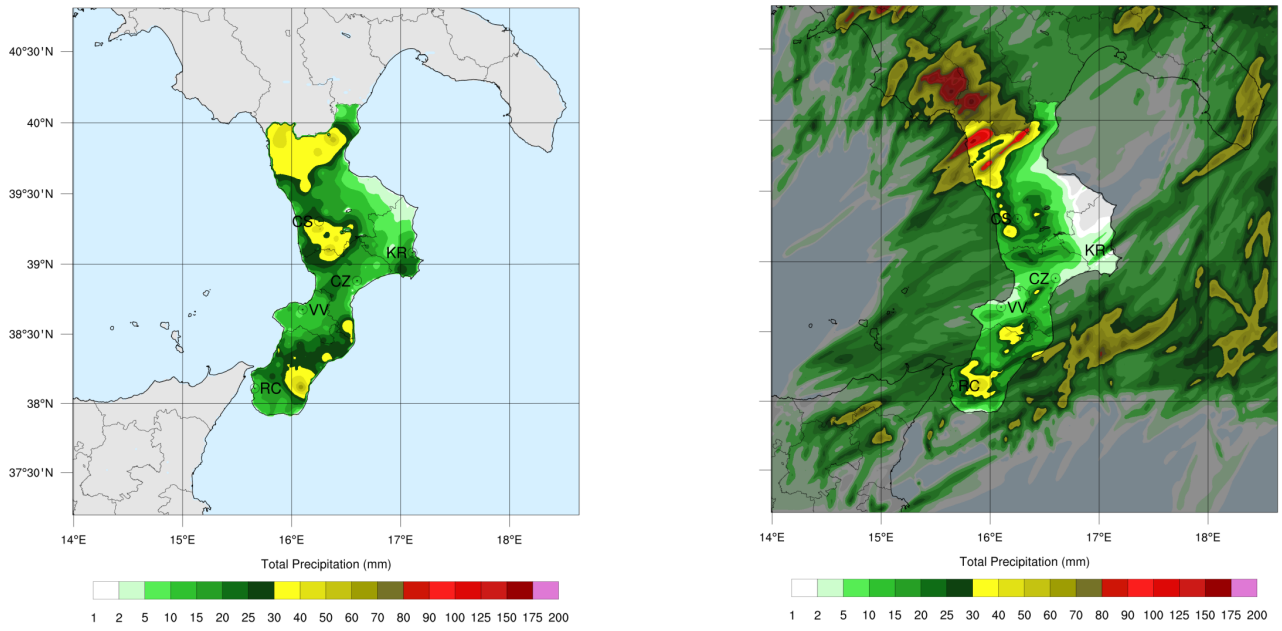

Figure S12. Cumulative precipitation for event 10: on the left, interpolated observation map; on the right, SST0 simulation.

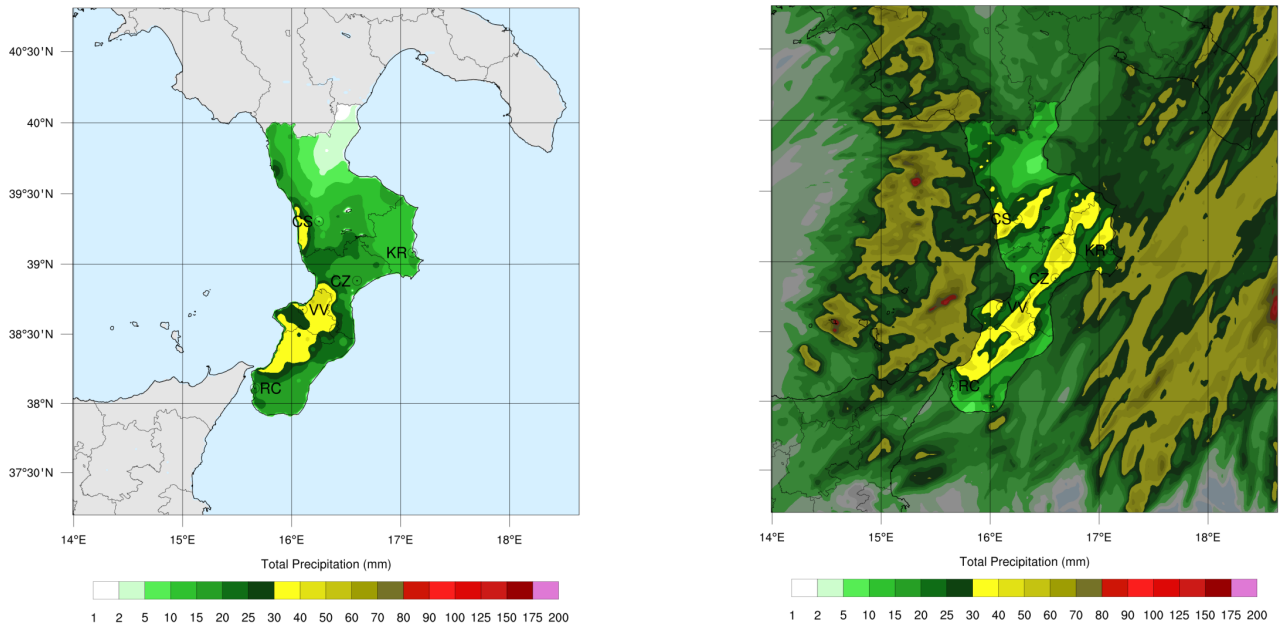

Figure S13. Cumulative precipitation for event 11: on the left, interpolated observation map; on the right, SST0 simulation.

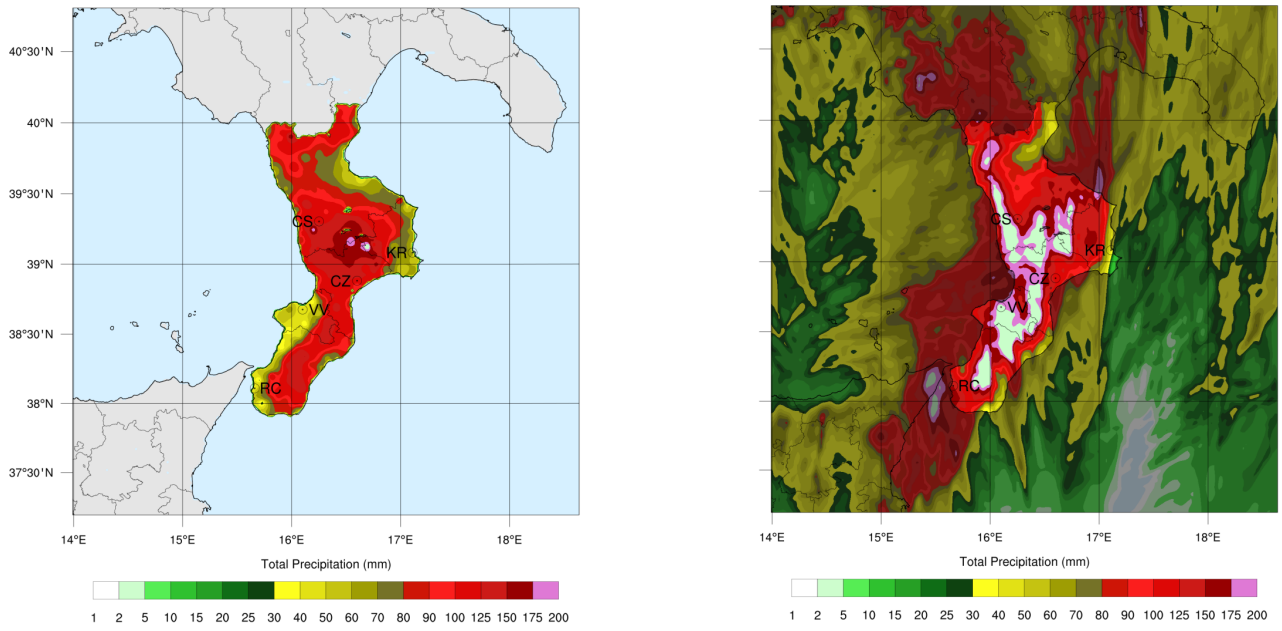

Figure S14. Cumulative precipitation for event 12: on the left, interpolated observation map; on the right, SST0 simulation.

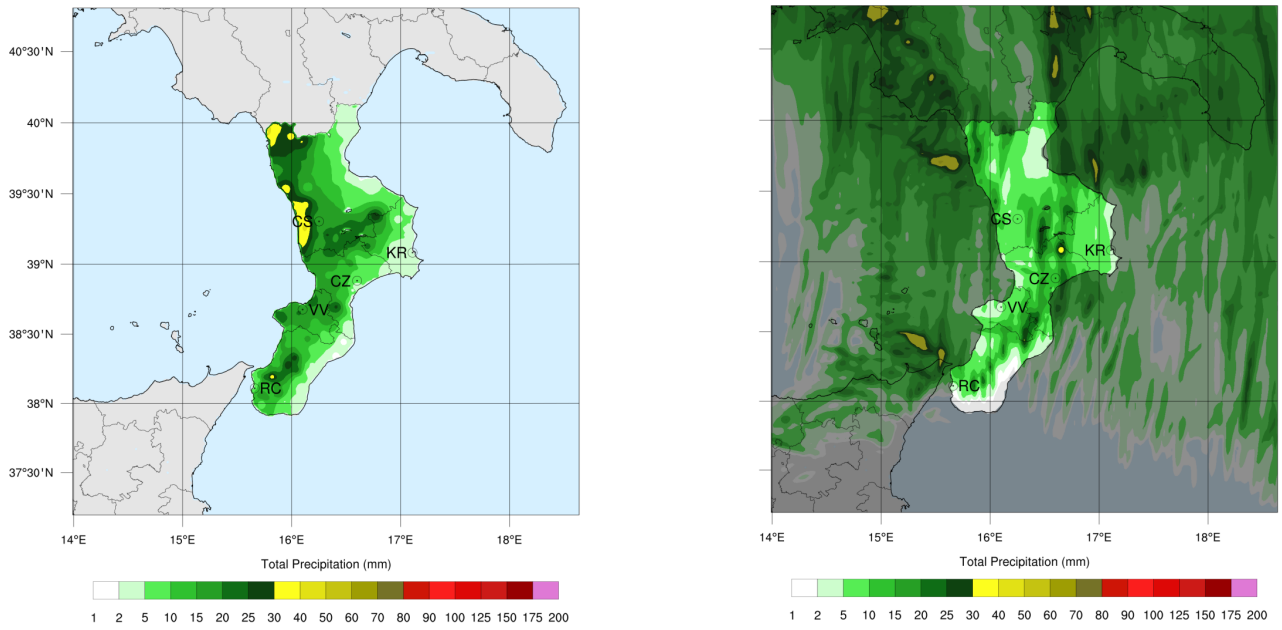

Figure S15. Cumulative precipitation for event 13: on the left, interpolated observation map; on the right, SST0 simulation.

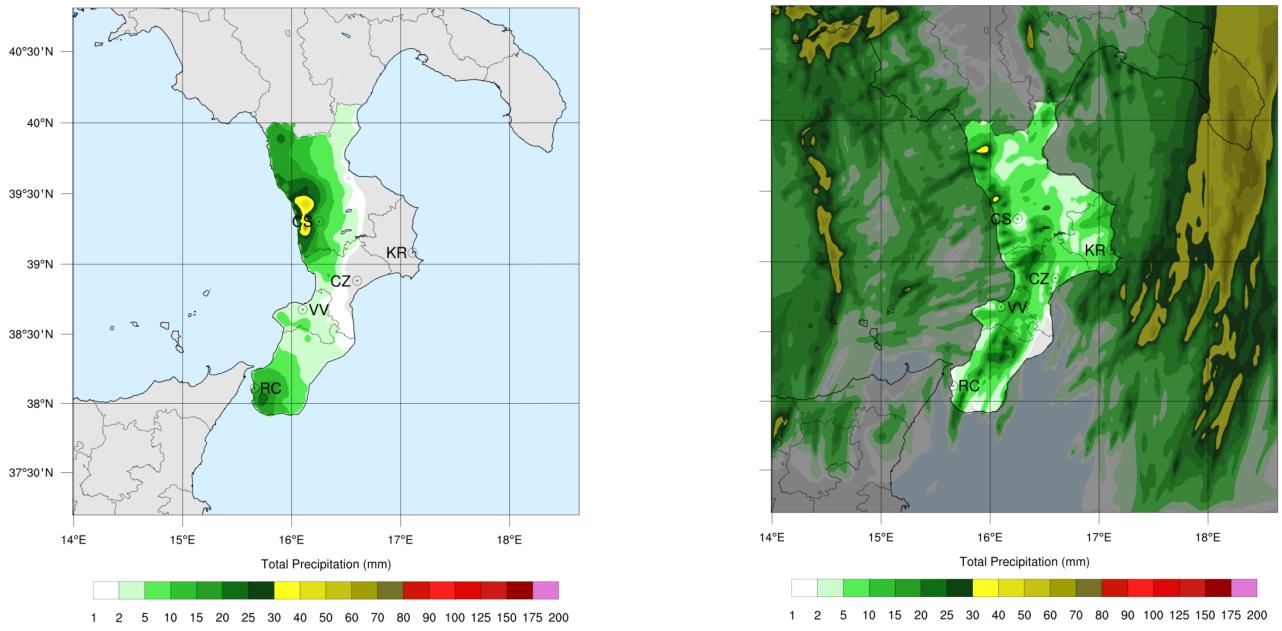

Figure S16. Cumulative precipitation for event 14: on the left, interpolated observation map; on the right, SST0 simulation.

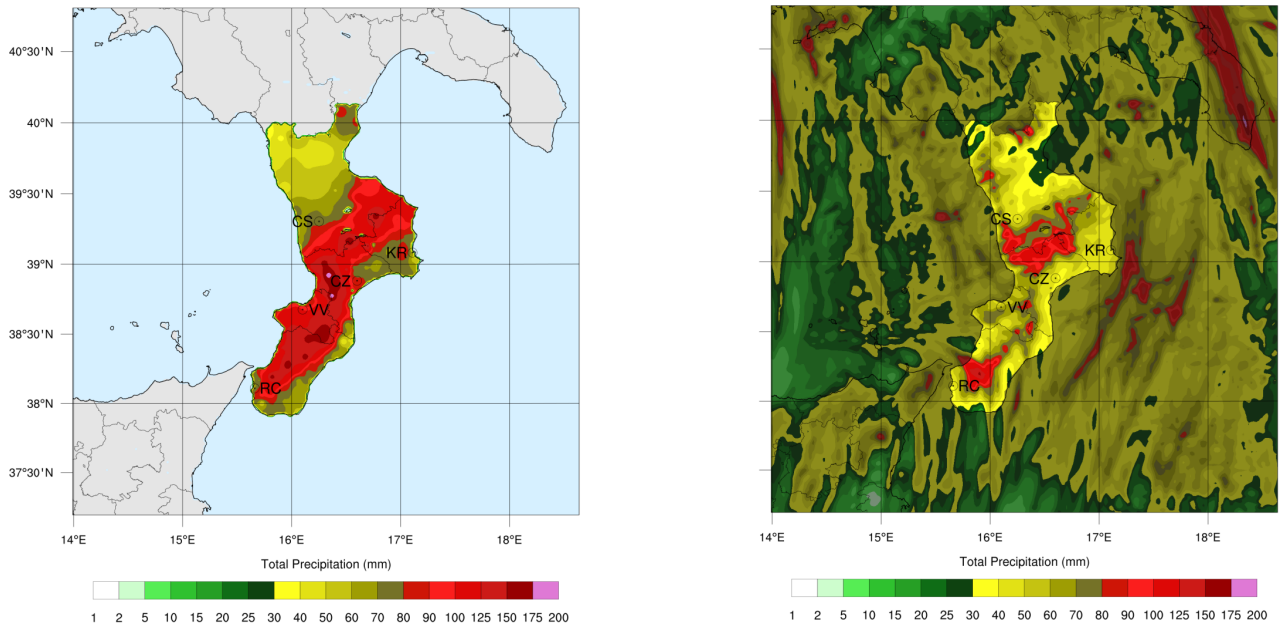

Figure S17. Cumulative precipitation for event 15: on the left, interpolated observation map; on the right, SST0 simulation.

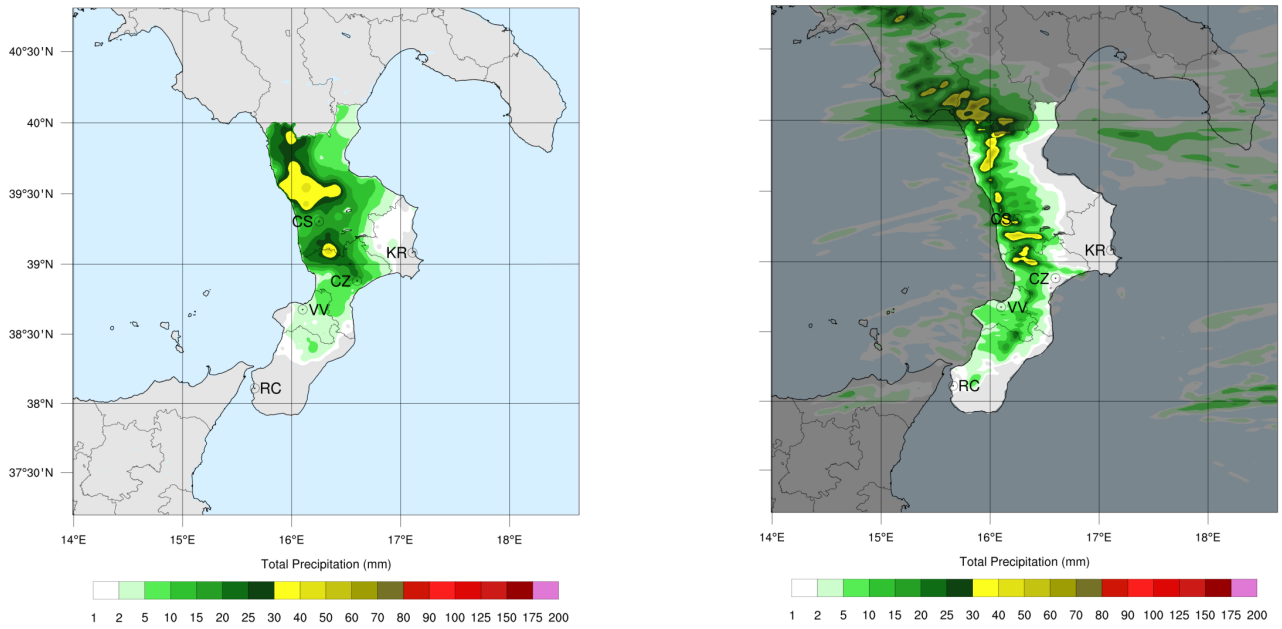

Figure S18. Cumulative precipitation for event 16: on the left, interpolated observation map; on the right, SST0 simulation.

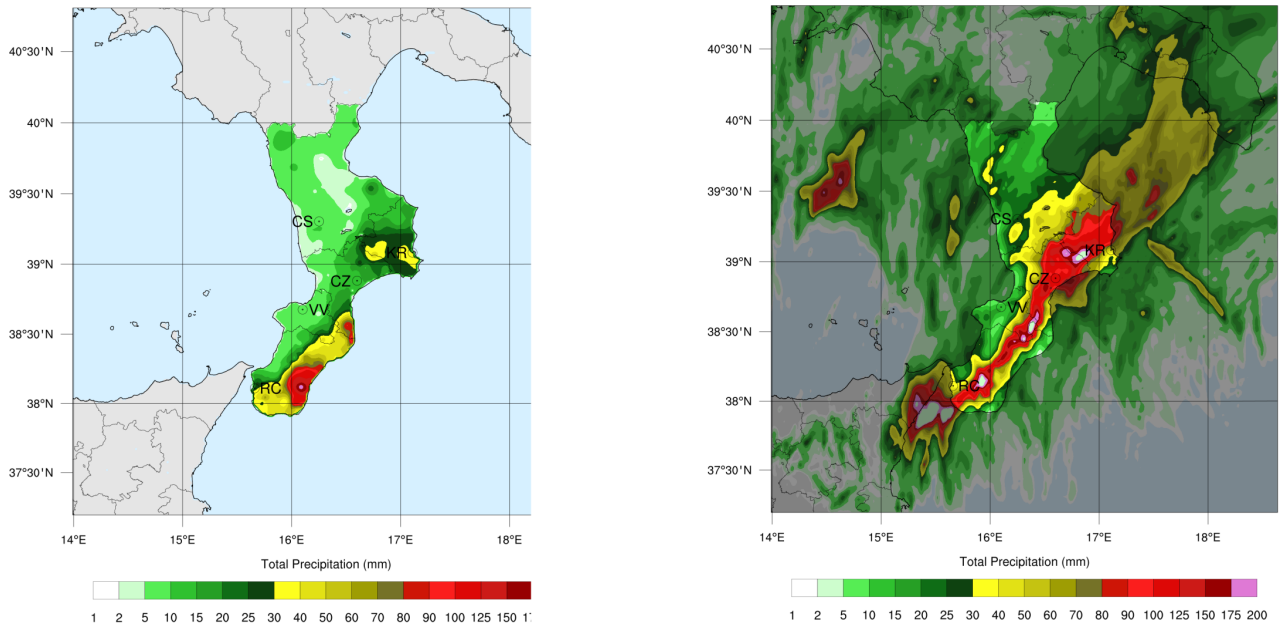

Figure S19. Cumulative precipitation for event 17: on the left, interpolated observation map; on the right, SST0 simulation.

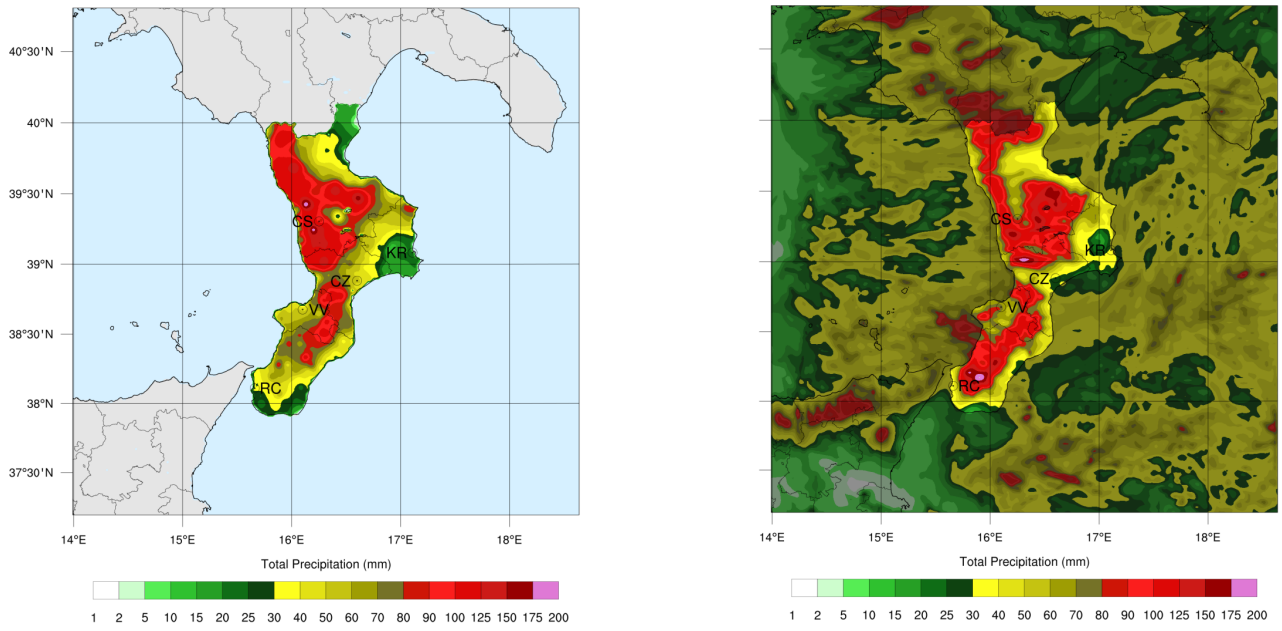

Figure S20. Cumulative precipitation for event 18: on the left, interpolated observation map; on the right, SST0 simulation.

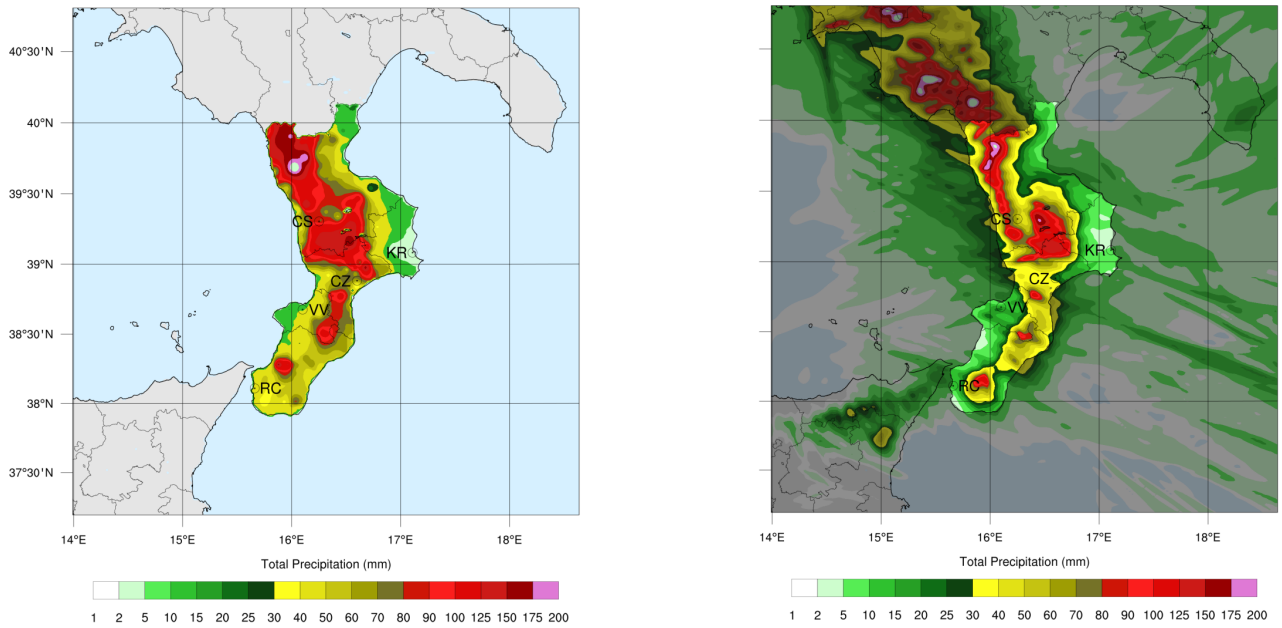

Figure S21. Cumulative precipitation for event 19: on the left, interpolated observation map; on the right, SST0 simulation.

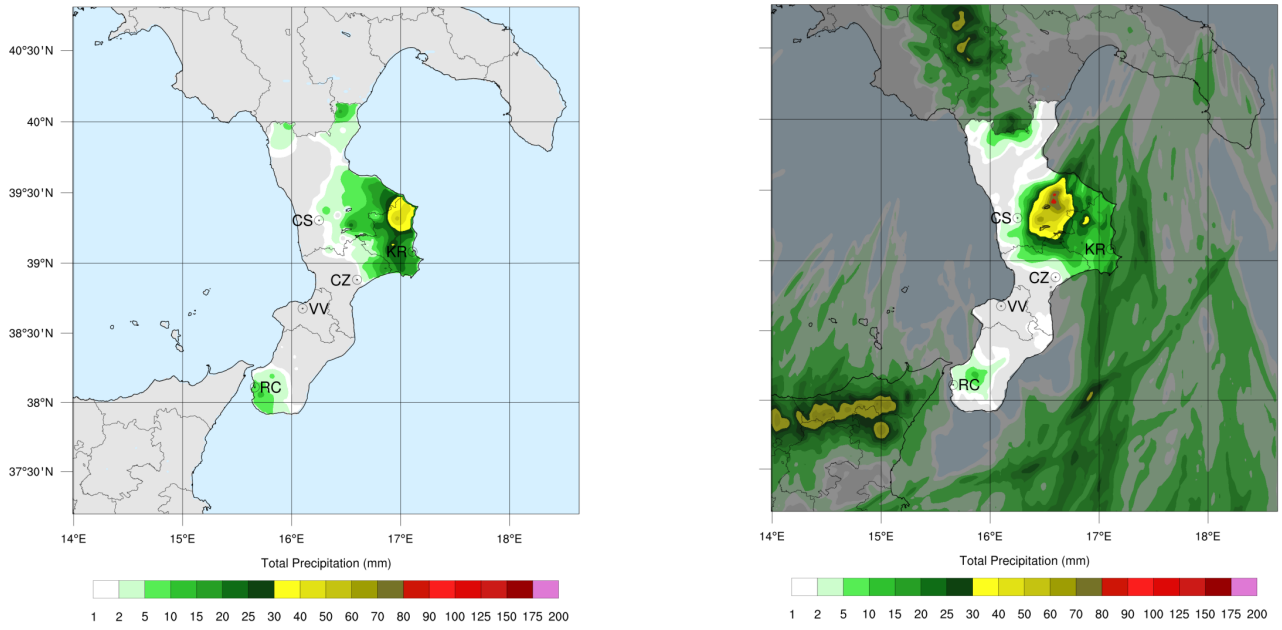

Figure S22. Cumulative precipitation for event 20: on the left, interpolated observation map; on the right, SST0 simulation.

ID	Start - End Date	n° days	$\bar{P}$ D02 SST0	$\bar{P}$ D02 SST-1	$\bar{P}$ D02 SST+3	$\bar{P}$ Land SST0	$\bar{P}$ land SST-1	$\bar{P}$ land SST+3	$\bar{P} > 95^{th}$ SST0	$\bar{P} > 95^{th}$ SST-1	$\bar{P} > 95^{th}$ SST+3
1	09/09-11/09	3	10.4	4.7	23.8	13.6	9.1	26.3	71.7	48.9	121.9
2	19/09-20/09	2	6.2	3.0	14.2	13.4	8.4	15.3	45.1	31.7	70.8
3	23/09-24/09	2	2.1	1.6	12.4	2.7	1.9	19.3	23.9	25.1	90.7
4	26/09-27/09	2	2.0	1.0	4.0	4.0	2.8	5.9	23.2	13.9	32.1
5	03/10-03/10	1	14.7	13.2	18.4	15.1	13.4	16.5	51.7	49.9	84.9
6	05/10-09/10	5	27.9	22.5	53.7	32.1	25.4	43.9	138.0	99.4	228.1
7	16/10-16/10	1	0.5	0.3	5.5	1.5	0.9	7.2	8.6	5.4	49.5
8	25/10-26/10	2	15.1	11.8	22.1	20.2	21.3	28.7	161.1	151.6	170.7
9	30/10-01/11	3	10.7	6.0	20.5	11.5	9.3	17.2	56.4	40.1	116.5
10	02/11-04/11	3	11.4	9.0	26.4	17.7	15.6	28.5	69.7	54.0	148.6
11	06/11-07/11	2	20.7	19.9	30.0	18.9	18.3	25.1	54.8	55.5	91.9
12	09/11-13/11	5	53.4	48.1	68.1	88.2	80.1	81.7	189.2	170.9	254.1
13	17/11-17/11	1	7.8	7.1	12.1	10.2	9.6	15.1	26.0	23.8	48.5
14	19/11-20/11	2	11.9	9.4	18.5	9.0	4.3	19.4	48.8	57.5	65.6
15	24/11-26/11	3	39.6	37.3	42.6	43.1	42.9	48.1	98.2	86.5	112.7
16	28/11-30/11	3	1.7	1.2	4.0	4.2	3.3	7.7	23.3	18.2	35.7
17	03/12-06/12	4	14.6	10.2	21.9	21.9	19.4	16.4	111.8	85.7	156.7
18	09/12-14/12	6	37.5	32.4	44.4	50.6	47.3	49.3	111.3	102.3	118.6
19	19/12-23/12	5	12.2	10.8	23.9	29.8	26.8	50.8	103.5	95.2	156.8
20	28/12-30/12	3	4.8	3.5	8.9	7.5	5.9	12.0	28.6	23.6	46.5

Table S3. Main features of the events identified in the analyzed period: event ID; starting and ending dates; duration in number of days; average precipitation $\bar{P}$ in the innermost D02 domain simulated by SST0, SST-1, and SST+3 scenarios, respectively; average overland precipitation $\bar{P}$ simulated by SST0, SST-1, and SST+3 scenarios, respectively; average of the accumulated precipitation $\bar{P}$ exceeding the 95th percentile simulated by SST0, SST-1, and SST+3 scenarios, respectively. All values are expressed in mm.

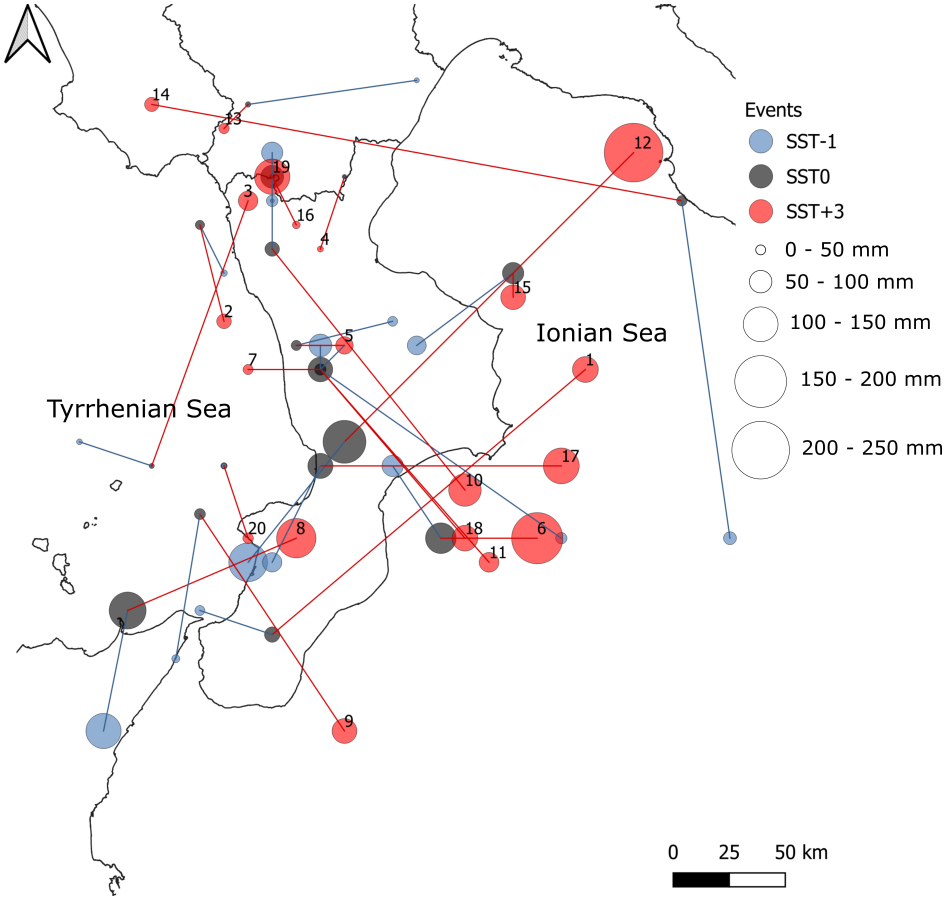

Figure S23. Locations of the centers of mass of the accumulated precipitation exceeding the 95th percentile for the 20 analyzed events, considering the outermost domain D01, with SST-1 (blue filled circles), SST0 (dark grey), and SST+3 (red).

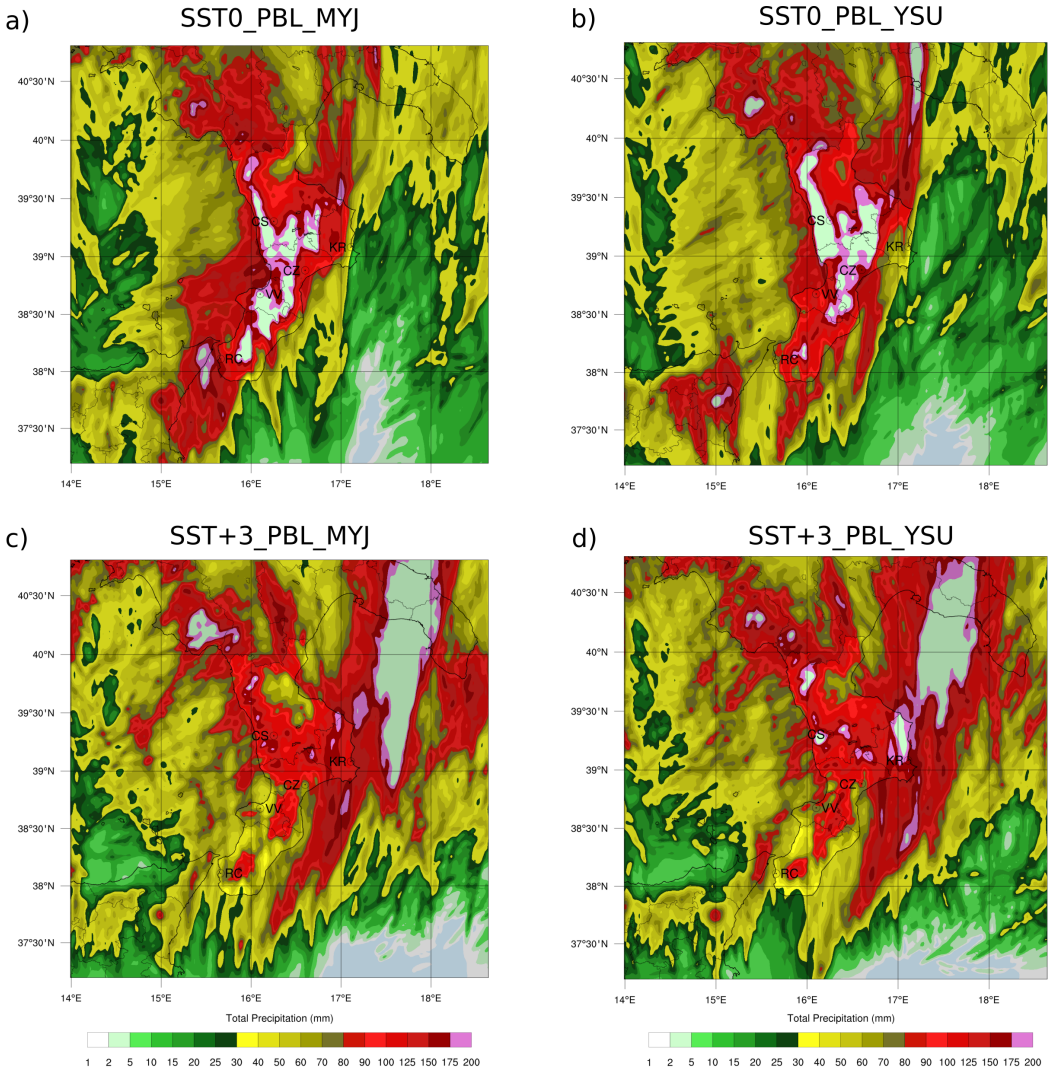

Figure S24. Cumulative precipitation for event no. 12 by changing the PBL scheme for the two SST Scenarios: a) and b): SST0; c) and d): SST+3. Results shown in a) and c) use the MYJ Scheme, those in b) and d) the YSU scheme.

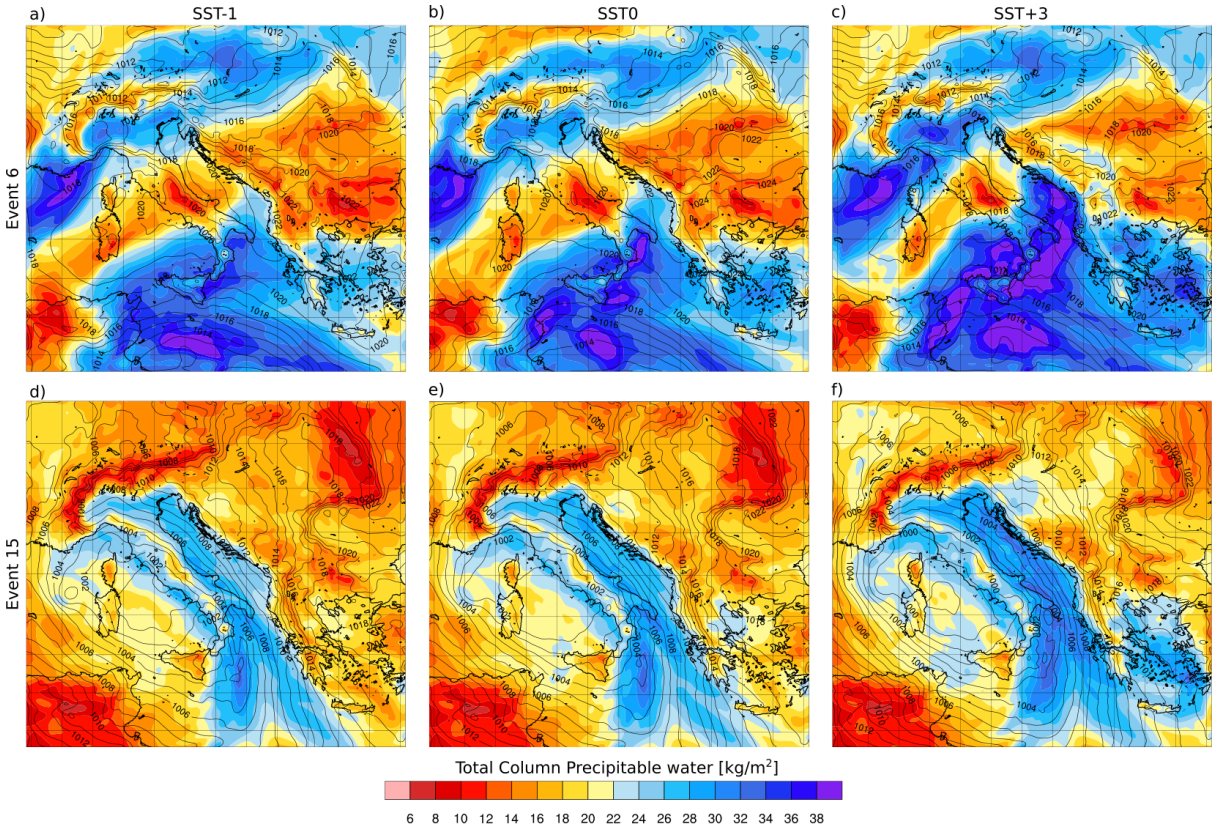

Figure S25. Column precipitable water (kg m^{-2}) for configurations SST-1 (a, d), SST0 (b, e), and SST+3 (c, f) during the events no. 6 on 6 October 2019 at 09:00 GMT (a–c), and event no. 15 on 24 November 2019 at 12:00 GMT (d–f). Sea level pressure (hPa) is also represented with contours.

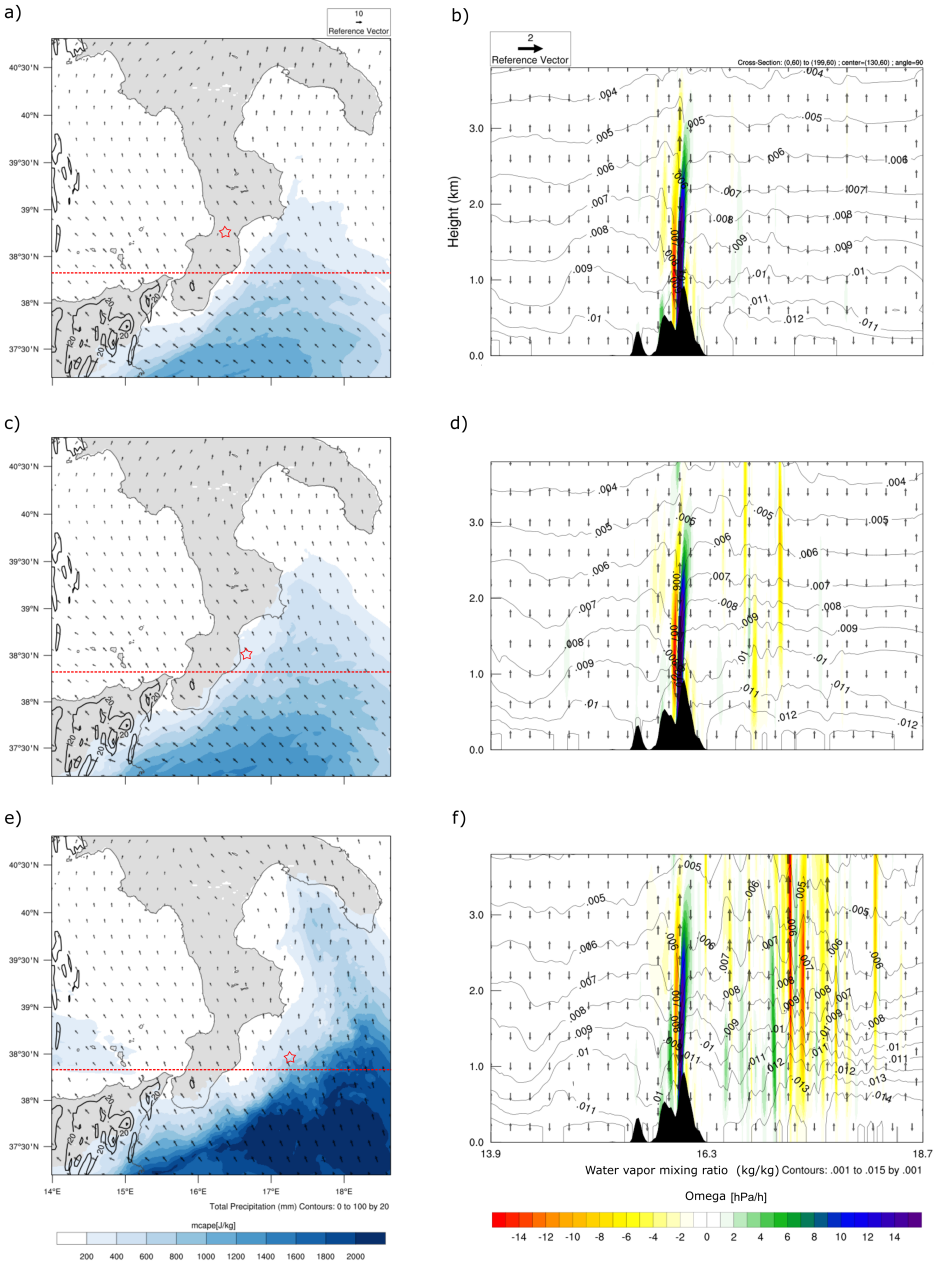

Figure S26. Left: Average CAPE (color bar), horizontal average wind at 850 hpa (arrows), and precipitation (isolines) during the eight hours preceding the most intense rainfall during event no. 6: a) SST-1, c) SST0, e) SST+3. The red star indicates the center of mass previously shown in Fig. 7 in the main text, while the red lines indicate the sections at which the vertical profiles were computed. Right: vertical profile of omega (color bar), water vapor mixing ratio (isolines), and vertical wind (upward or downward arrows for direction; speed proportional to the reference vector) for b) SST-1, d) SST0, f) SST+3.

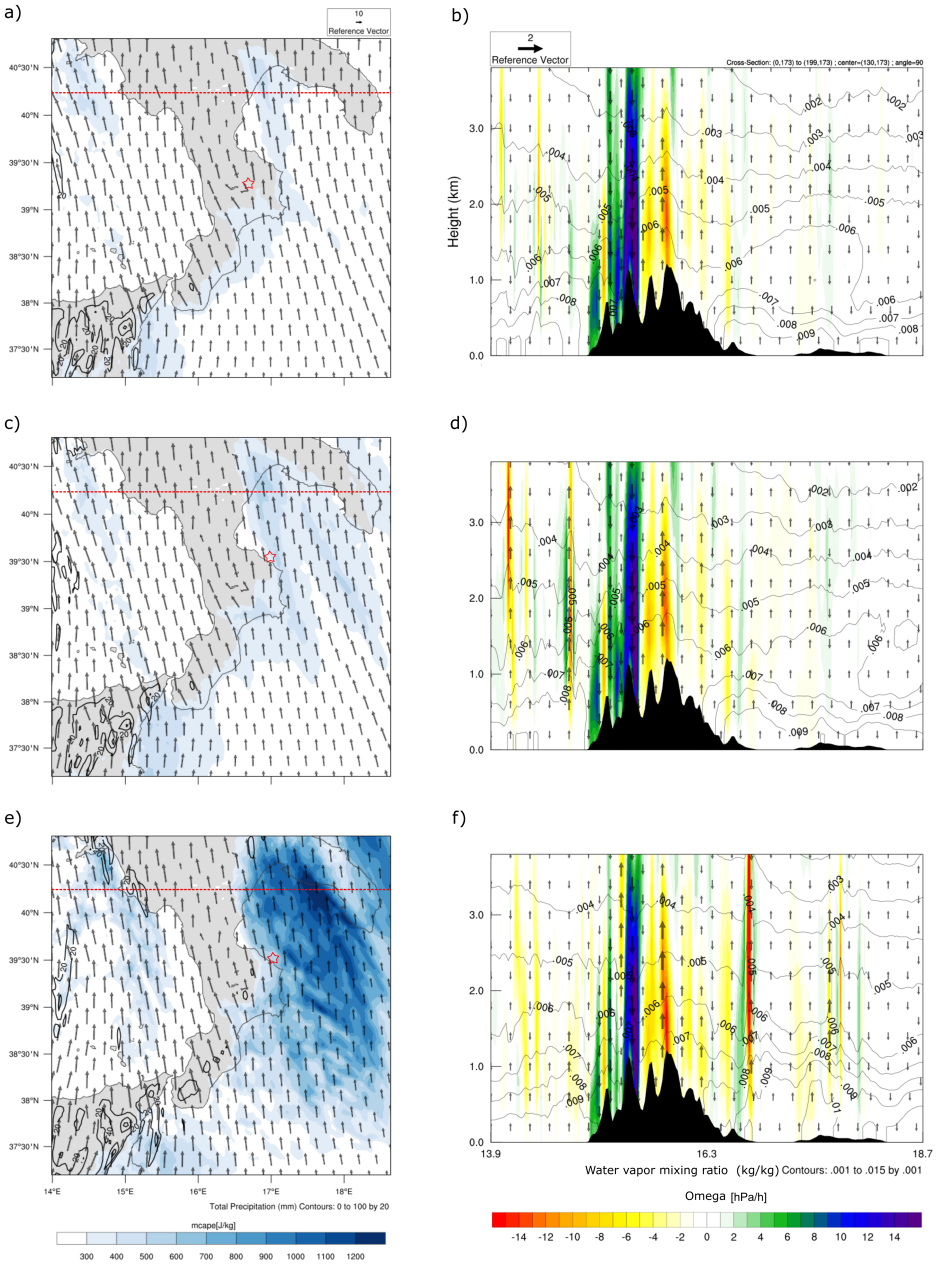

Figure S27. Left: Average CAPE (color bar), horizontal average wind at 850 hpa (arrows), and precipitation (isolines) during the six hours preceding the most intense rainfall during event no. 15: a) SST-1, c) SST0, e) SST+3. The red star indicates the center of mass previously shown in Fig. 7 in the main text, while the red lines indicate the sections at which the vertical profiles were computed. Right: vertical profile of omega (color bar), water vapor mixing ratio (isolines), and vertical wind (upward or downward arrows for direction; speed proportional to the reference vector) for b) SST-1, d) SST0, f) SST+3.

References

Aguilar, E., Peterson, T. C., Obando, P. R., Frutos, R., Retana, J. A., Solera, M., Soley, J., García, I. G., Araujo, R. M., Santos, A. R., Valle, V. E., Brunet, M., Aguilar, L., Álvarez, L., Bautista, M., Castañón, C., Herrera, L., Ruano, E., Sinay, J. J., Sánchez, E., Oviedo, G. I. H., Obed, F., Salgado, J. E., Vázquez, J. L., Baca, M., Gutiérrez, M., Centella, C., Espinosa, J., Martínez, D., Olmedo, B., Espinoza, C. E. O., Núñez, R., Haylock, M., Benavides, H., and Mayorga, R.: Changes in precipitation and temperature extremes in Central America and northern South America, 1961–2003, Journal of Geophysical Research: Atmospheres, 110, https://doi.org/https://doi.org/10.1029/2005JD006119, 2005.

Bentsen, M., Oliviè, D. J. L., Seland, y., Toniazzo, T., Gjermundsen, A., Graff, L. S., Debernard, J. B., Gupta, A. K., He, Y., Kirkevåg, A., Schwinger, J., Tjiputra, J., Aas, K. S., Bethke, I., Fan, Y., Griesfeller, J., Grini, A., Guo, C., Ilicak, M., Karset, I. H. H., Landgren, O. A., Liakka, J., Moseid, K. O., Nummelin, A., Spensberger, C., Tang, H., Zhang, Z., Heinze, C., Iversen, T., and Schulz, M.: IPCC DDC: NCC NorESM2-MM model output prepared for CMIP6 CMIP, https://doi.org/10.26050/WDCC/AR6.C6CMNCCN2, 2023.

Boucher, O., Denvil, S., Levavasseur, G., Cozic, A., Caubel, A., Foujols, M.-A., Meurdesoif, Y., Cadule, P., Devilliers, M., Ghattas, J., Lebas, N., Lurton, T., Mellul, L., Musat, I., Mignot, J., and Cheruy, F.: IPCC DDC: IPSL IPSL-CM6A-LR model output prepared for CMIP6 CMIP, https://doi.org/10.26050/WDCC/AR6.C6CMIPICL, 2023.

(CMEMS), E. C. M. S. I.: ESA SST CCI and C3S reprocessed sea surface temperature analyses, https://doi.org/doi.org/10.48670/moi-00169, accessed on 09-Oct-2024, 2023.

Danabasoglu, G.: IPCC DDC: NCAR CESM2-WACCM model output prepared for CMIP6 CMIP, https://doi.org/10.26050/WDCC/AR6.C6CMNRCESWA, 2023.

Dix, M., Bi, D., Dobrohotoff, P., Fiedler, R., Harman, I., Law, R., Mackallah, C., Marsland, S., O'Farrell, S., Rashid, H., Srbinovsky, J., Sullivan, A., Trenham, C., Vohralik, P., Watterson, I., Williams, G., Woodhouse, M., Bodman, R., Dias, F. B., Domingues, C. M., Hannah, N., Heerdegen, A., Savita, A., Wales, S., Allen, C., Druken, K., Evans, B., Richards, C., Ridzwan, S. M., Roberts, D., Smillie, J., Snow, K., Ward, M., and Yang, R.: IPCC DDC: CSIRO-ARCCSS ACCESS-CM2 model output prepared for CMIP6 CMIP, https://doi.org/10.26050/WDCC/AR6.C6CMCSIACC, 2023.

Donat, M. G., Alexander, L. V., Yang, H., Durre, I., Vose, R., Dunn, R. J. H., Willett, K. M., Aguilar, E., Brunet, M., Caesar, J., Hewitson, B., Jack, C., Klein Tank, A. M. G., Kruger, A. C., Marengo, J., Peterson, T. C., Renom, M., Oria Rojas, C., Rusticucci, M., Salinger, J., Elrayah, A. S., Sekele, S. S., Srivastava, A. K., Trewin, B., Villarroel, C., Vincent, L. A., Zhai, P., Zhang, X., and Kitching, S.: Updated analyses of temperature and precipitation extreme indices since the beginning of the twentieth century: The HadEX2 dataset, Journal of Geophysical Research: Atmospheres, 118, 2098–2118, https://doi.org/https://doi.org/10.1002/jgrd.50150, 2013.

(EC-Earth), E.-E. C.: IPCC DDC: EC-Earth-Consortium EC-Earth-3-CC model output prepared for CMIP6 CMIP, https://doi.org/10.26050/WDCC/AR6.C6CMEEEEC, 2023.

Hersbach, H., Bell, B., Berrisford, P., Hirahara, S., Horányi, A., Muñoz-Sabater, J., Nicolas, J., Peubey, C., Radu, R., Schepers, D., et al.: The ERA5 global reanalysis, Quarterly Journal of the Royal Meteorological Society, 146, 1999–2049, https://doi.org/10.1002/qj.3803, 2020.

Instituto de Física de Cantabria (IFCA), C.: IPCC-WGI AR6 Interactive Atlas Dataset: CMIP6, https://doi.org/10.20350/digitalCSIC/15492, 2023.

Janjić, Z. I.: The Step-Mountain Eta Coordinate Model: Further Developments of the Convection, Viscous Sublayer, and Turbulence Closure Schemes, Monthly weather review, 122, 927–945, https://doi.org/10.1175/1520-0493(1994)122<0927:TSMECM>2.0.CO;2, 1994.

Jungclaus, J., Bittner, M., Wieners, K.-H., Wachsmann, F., Schupfner, M., Legutke, S., Giorgetta, M., Reick, C., Gayler, V., Haak, H., de Vrese, P., Raddatz, T., Esch, M., Mauritsen, T., von Storch, J.-S., Behrens, J., Brovkin, V., Claussen, M., Crueger, T., Fast, I., Fiedler, S., Hagemann, S., Hohenegger, C., Jahns, T., Kloster, S., Kinne, S., Lasslop, G., Kornblueh, L., Marotzke, J., Matei, D., Meraner, K., Mikolajewicz, U., Modali, K., Müller, W., Nabel, J., Notz, D., Peters-von Gehlen, K., Pincus, R., Pohlmann, H., Pongratz, J., Rast, S., Schmidt, H., Schnur, R., Schulzweida, U., Six, K., Stevens, B., Voigt, A., and Roeckner, E.: IPCC DDC: MPI-M MPIESM1.2-HR model output prepared for CMIP6 CMIP, https://doi.org/10.26050/WDCC/AR6.C6CMMXME2, 2023.

Krasting, J. P., John, J. G., Blanton, C., McHugh, C., Nikonov, S., Radhakrishnan, A., Rand, K., Zadeh, N. T., Balaji, V., Durachta, J., Dupuis, C., Menzel, R., Robinson, T., Underwood, S., Vahlenkamp, H., Dunne, K. A., Gauthier, P. P., Ginoux, P., Griffies, S. M., Hallberg, R., Harrison, M., Hurlin, W., Malyshev, S., Naik, V., Paulot, F., Paynter, D. J., Ploshay, J., Reichl, B. G., Schwarzkopf, D. M., Seman, C. J., Silvers, L., Wyman, B., Zeng, Y., Adcroft, A., Dunne, J. P., Dussin, R., Guo, H., He, J., Held, I. M., Horowitz, L. W., Lin, P., Milly, P., Shevliakova, E., Stock, C., Winton, M., Wittenberg, A. T., Xie, Y., and Zhao, M.: IPCC DDC: NOAA-GFDL GFDL-ESM4 model output prepared for CMIP6 CMIP, https://doi.org/10.26050/WDCC/AR6.C6CMNGGFE, 2023.

Li, L.: IPCC DDC: CAS FGOALS-g3 model output prepared for CMIP6 ScenarioMIP, https://doi.org/10.26050/WDCC/AR6.C6SPCASFGO, 2023.

Lovato, T. and Peano, D.: IPCC DDC: CMCC CMCC-CM2-SR5 model output prepared for CMIP6 CMIP, https://doi.org/10.26050/WDCC/AR6.C6CMCMCCS, 2023.

Matsui, T., Zhang, S. Q., Lang, S. E., Tao, W.-K., Ichoku, C., and Peters-Lidard, C. D.: Impact of radiation frequency, precipitation radiative forcing, and radiation column aggregation on convection-permitting West African monsoon simulations, Climate Dynamics, 55, 193–213, https://doi.org/10.1007/s00382-018-4187-2, 2020.

Mlawer, E. J., Taubman, S. J., Brown, P. D., Iacono, M. J., and Clough, S. A.: Radiative transfer for inhomogeneous atmospheres: RRTM, a validated correlated-k model for the longwave, Journal of Geophysical Research: Atmospheres, 102, 16 663–16 682, https://doi.org/10.1029/97JD00237, 1997.

Niu, G.-Y., Yang, Z.-L., Mitchell, K. E., Chen, F., Ek, M. B., Barlage, M., Kumar, A., Manning, K., Niyogi, D., Rosero, E., et al.: The community Noah land surface model with multiparameterization options (Noah-MP): 1. Model description and evaluation with local-scale measurements, Journal of Geophysical Research: Atmospheres, 116, https://doi.org/10.1029/2010JD015139, 2011.

Panickal, S., Raghavan, K., Gopinathan, P. A., Narayanasetti, S., Choudhury, A. D., Singh, M., and Modi, A.: IPCC DDC: CCCR-IITM IITM-ESM model output data prepared for CMIP6 CMIP/DECK, https://doi.org/10.26050/WDCC/AR6.C6CMCIIIT, 2023.

Rong, X.: IPCC DDC: CAMS CAMS_CSM1.0 model output prepared for CMIP6 CMIP, https://doi.org/10.26050/WDCC/AR6.C6CMCAMCC0, 2023.

Seferian, R.: IPCC DDC: CNRM-CERFACS CNRM-ESM2-1 model output prepared for CMIP6 CMIP, https://doi.org/10.26050/WDCC/AR6.C6CMCECE1, 2023.

Seland, y., Bentsen, M., Oliviè, D. J. L., Toniazzo, T., Gjermundsen, A., Graff, L. S., Debernard, J. B., Gupta, A. K., He, Y., Kirkevåg, A., Schwinger, J., Tjiputra, J., Aas, K. S., Bethke, I., Fan, Y., Griesfeller, J., Grini, A., Guo, C., Ilicak, M., Karset, I. H. H., Landgren, O. A., Liakka, J., Moseid, K. O., Nummelin, A., Spensberger, C., Tang, H., Zhang, Z., Heinze, C., Iversen, T., and Schulz, M.: IPCC DDC: NCC NorESM2-LM model output prepared for CMIP6 CMIP, https://doi.org/10.26050/WDCC/AR6.C6CMNCCNL, 2023.

Semmler, T., Danilov, S., Rackow, T., Sidorenko, D., Barbi, D., Hegewald, J., Sein, D., Wang, Q., and Jung, T.: IPCC DDC: AWI AWI-CM1.1MR model output prepared for CMIP6 CMIP, https://doi.org/10.26050/WDCC/AR6.C6CMAWAWM, 2023.

Stephenson, T. S., Vincent, L. A., Allen, T., Van Meerbeeck, C. J., McLean, N., Peterson, T. C., Taylor, M. A., Aaron-Morrison, A. P., Auguste, T., Bernard, D., Boekhoudt, J. R. I., Blenman, R. C., Braithwaite, G. C., Brown, G., Butler, M., Cumberbatch, C. J. M., Etienne-Leblanc, S., Lake, D. E., Martin, D. E., McDonald, J. L., Ozoria Zaruela, M., Porter, A. O., Santana Ramirez, M., Tamar, G. A., Roberts, B. A., Sallons Mitro, S., Shaw, A., Spence, J. M., Winter, A., and Trotman, A. R.: Changes in extreme temperature and precipitation in the Caribbean region, 1961–2010, International Journal of Climatology, 34, 2957–2971, https://doi.org/https://doi.org/10.1002/joc.3889, 2014.

Swart, N. C., Cole, J. N., Kharin, V. V., Lazare, M., Scinocca, J. F., Gillett, N. P., Anstey, J., Arora, V., Christian, J. R., Jiao, Y., Lee, W. G., Majaess, F., Saenko, O. A., Seiler, C., Seinen, C., Shao, A., Solheim, L., von Salzen, K., Yang, D., Winter, B., and Sigmond, M.: IPCC DDC: CCCma CanESM5 model output prepared for CMIP6 CMIP, https://doi.org/10.26050/WDCC/AR6.C6CMCCCE, 2023.

Tang, Y., Rumbold, S., Ellis, R., Kelley, D., Mulcahy, J., Sellar, A., Walton, J., and Jones, C.: IPCC DDC: MOHC UKESM1.0-LL model output prepared for CMIP6 CMIP, https://doi.org/10.26050/WDCC/AR6.C6CMMOU0, 2023.

Thompson, G., Field, P. R., Rasmussen, R. M., and Hall, W. D.: Explicit Forecasts of Winter Precipitation Using an Improved Bulk Microphysics Scheme. Part II: Implementation of a New Snow Parameterization, Monthly Weather Review, 136, 5095–5115, https://doi.org/10.1175/2008MWR2387.1, 2008.

Tiedtke, M.: A Comprehensive Mass Flux Scheme for Cumulus Parameterization in Large-Scale Models, Monthly weather review, 117, 1779–1800, https://doi.org/10.1175/1520-0493(1989)117<1779:ACMFSF>2.0.CO;2, 1989.

Voldoire, A.: IPCC DDC: CNRM-CERFACS CNRM-CM6-1-HR model output prepared for CMIP6 CMIP, https://doi.org/10.26050/WDCC/AR6.C6CMCECC2, 2023a.

Voldoire, A.: IPCC DDC: CNRM-CERFACS CNRM-CM6-1 model output prepared for CMIP6 CMIP, https://doi.org/10.26050/WDCC/AR6.C6CMCECC1, 2023b.

Volodin, E., Mortikov, E., Gritsun, A., Lykossov, V., Galin, V., Diansky, N., Gusev, A., Kostrykin, S., Iakovlev, N., Shestakova, A., and Emelina, S.: IPCC DDC: INM INM-CM5-0 model output prepared for CMIP6 CMIP, https://doi.org/10.26050/WDCC/AR6.C6CMINIC0, 2023.

Wieners, K.-H., Giorgetta, M., Jungclaus, J., Reick, C., Esch, M., Bittner, M., Legutke, S., Schupfner, M., Wachsmann, F., Gayler, V., Haak, H., de Vrese, P., Raddatz, T., Mauritsen, T., von Storch, J.-S., Behrens, J., Brovkin, V., Claussen, M., Crueger, T., Fast, I., Fiedler, S., Hagemann, S., Hohenegger, C., Jahns, T., Kloster, S., Kinne, S., Lasslop, G., Kornblueh, L., Marotzke, J., Matei, D., Meraner, K., Mikolajewicz, U., Modali, K., Müller, W., Nabel, J., Notz, D., Peters-von Gehlen, K., Pincus, R., Pohlmann, H., Pongratz, J., Rast, S., Schmidt, H., Schnur, R., Schulzweida, U., Six, K., Stevens, B., Voigt, A., and Roeckner, E.: PCC DDC: MPI-M MPIESM1.2-LR model output prepared for CMIP6 CMIP, https://doi.org/10.26050/WDCC/AR6.C6CMMXML2, 2023.

Xin, X., Zhang, J., Zhang, F., Wu, T., Shi, X., Li, J., Chu, M., Liu, Q., Yan, J., Ma, Q., and Wei, M.: IPCC DDC: BCC BCC-CSM2MR model output prepared for CMIP6 CMIP, https://doi.org/10.26050/WDCC/AR6.C6CMBCBCM, 2023.

Zeng, X. and Beljaars, A.: A prognostic scheme of sea surface skin temperature for modeling and data assimilation, Geophysical Research Letters, 32, https://doi.org/10.1029/2005GL023030, 2005.

Ziehn, T., Chamberlain, M., Lenton, A., Law, R., Bodman, R., Dix, M., Wang, Y., Dobrohotoff, P., Srbinovsky, J., Stevens, L., Vohralik, P., Mackallah, C., Sullivan, A., O'Farrell, S., and Druken, K.: IPCC DDC: CSIRO ACCESS-ESM1.5 model output prepared for CMIP6 CMIP, https://doi.org/10.26050/WDCC/AR6.C6CMCSAE, 2023.